Vol. 84: 197–214, 2021
https://doi.org/10.3354/cr01657

CLIMATE RESEARCH
Clim Res

Published online October 7

Backward trajectory analysis of southern California atmospheric rivers

Sarah M. Harris[1,*], Leila M. V. Carvalho[2,3]

[1]Department of Geography, McGill University, Montréal, QC H3A 3B3, Canada
[2]Department of Geography, University of California Santa Barbara, Santa Barbara, CA 93106, USA
[3]Earth Research Institute, Santa Barbara, CA 93106, USA

ABSTRACT: Atmospheric rivers (ARs) are filamentary channels of high water vapor flux that transfer moisture horizontally through the atmosphere at low levels. ARs are often responsible for large annual rainfall totals as well as high-intensity storms due to orographic forcing. ARs are important features when predicting hazardous events such as flooding and are vital components of many regional water budgets. This is especially true for drought-prone areas such as southern California (SCA), which experiences relatively few storms per season, many from AR events. Here, we use a Lagrangian model to create backward air parcel trajectories of 159 AR events that made landfall on the US west coast from December 2004 to December 2015. Trajectories are used to examine the lifecycles and movements of these ARs and to differentiate ARs that made landfall in different regions. Prior to landfall, SCA ARs share similarities to but also have distinct differences from other ARs. At 1000 m above mean sea level (MSL), SCA AR trajectories travel shorter distances over the same 72 h time frame than trajectories for ARs that made landfall farther north. Additionally, along-trajectory measurements for SCA ARs tend to be warmer and have higher specific humidity values. This applies to both the 1000 and 2000 m MSL levels. These results imply that SCA ARs move slower and have the potential to produce higher intensity storms at landfall. An analysis of a case study event of an extreme AR that made landfall in SCA on 17 February 2017 confirms these results.

KEY WORDS: Atmospheric rivers · Trajectories analysis · Extreme precipitation · Southern California

1. INTRODUCTION

Atmospheric rivers (ARs) are filamentary channels of high water vapor flux that form over oceans and transfer moisture horizontally through the atmosphere. They are typically defined with lengths over 2000 km and widths less than 1000 km along with integrated water vapor values meeting or exceeding 2 cm (Zhu & Newell 1994, 1998, Ralph et al. 2005, 2006, 2011, Neiman et al. 2008a,b). AR cores have warm temperatures as well as strong winds organized as wind jets leading to high water vapor flux with most vapor transport occurring in the lowest 2.5 km of the troposphere, an area of the atmosphere that tends to be moist and statically neutral (Neiman et al. 2002, Ralph et al. 2003, 2004, 2005, 2006, Neiman et al. 2008a, Dettinger et al. 2011, Ralph & Dettinger 2011, 2012). ARs can result in high-intensity precipitation, particularly along mountainous coastlines due to orographic forcing upon landfall (Neiman et al. 2002, Ralph et al. 2005, Neiman et al. 2008a, Ralph & Dettinger 2011, 2012, Martinković et al. 2017).

Early studies found that ARs were responsible for up to 90% of global meridional water vapor movement (Newell et al. 1992, Zhu & Newell 1994, 1998, Ralph et al. 2004, Neiman et al. 2008a,b). Moisture

*Corresponding author: sarah.harris@mcgill.ca

transport can occur in conjunction with extratropical cyclones, with convergence along the leading edge of the cold front leading to continuous cycling of water vapor (Bao et al. 2006, Newman et al. 2012, Sodemann & Stohl 2013, Martinković et al. 2017). It is also possible for direct moisture transport over large distances with limited gains/losses of water vapor along the trajectory due to precipitation (e.g. Bao et al. 2006, Knippertz & Martin 2007, Ralph et al. 2011). ARs are important components of many regional water budgets, and forecasts of ARs are imperative, as the high-intensity precipitation associated with AR events are often connected to hazards such as flooding (e.g. Ralph et al. 2006, Neiman et al. 2008b, 2011, Leung & Qian 2009, Knippertz & Wernli 2010, Dettinger et al. 2011, Lavers et al. 2011, Ralph & Dettinger 2011, Konrad & Dettinger 2017).

Previous AR studies have focused on events that affected the western coast of North America, and some have investigated the connections between AR precipitation and local hazards (e.g. Dettinger 2004, Dettinger et al. 2011, Neiman et al. 2011, Ralph & Dettinger 2012). In this region, ARs are significant contributors to annual water cycles (Dettinger et al. 2011, Ralph & Dettinger 2012); however, their frequency and intensity varies by landfall location (Gershunov et al. 2017). Southern California (SCA) is an area along North America's west coast that is particularly sensitive to rainfall changes, with annual precipitation totals often achieved from only a few events per season indicating high rainfall event variability (Dettinger et al. 2011, Kim et al. 2013, Oakley et al. 2018). SCA is also an area very susceptible to extreme rainfall and is prone to various precipitation-induced hazardous events including flooding and landslides, particularly in landscapes affected by wildfire. Previous studies found that ARs made up a large proportion of the region's annual precipitation events as well as totals (Dettinger et al. 2011, Rutz & Steenburgh 2012, Kim et al. 2013). Thus, any changes to AR frequencies and/or intensities may have dramatic consequences for the region's population and environment. Yet most studies have focused on the northern reaches of the continent and few have considered the characteristics of AR events that make landfall in SCA (e.g. Harris & Carvalho 2018). According to Neiman et al. (2008a), ARs that landfall along North America's west coast vary in terms of trajectories, sources, and intensities.

SCA ARs, like their more northern counterparts, are characterized by baroclinic midlatitude wave trains progressing through the Pacific. This process leads to northeastward-oriented moisture plumes with an accompanying offshore trough and onshore ridge along with lower tropospheric warming and southwesterly flow on landfall days (Neiman et al. 2008a, Harris & Carvalho 2018). However, SCA ARs are less frequent than those making landfall farther north, and AR-related moisture appears farther eastward and southward over the Pacific (Neiman et al. 2008a,b, Kim et al. 2013, Harris & Carvalho 2018).

Harris & Carvalho (2018) concluded that in the days directly prior to an AR landfall, there is a 500 mb trough over the eastern coast of Asia and an accompanying ridge over Alaska for all ARs that make landfall in western North America, consistent with baroclinic wave theory. For ARs that make landfall in SCA, the trough is deeper, and the ridge is amplified. They also found that when this deep trough and amplified ridge occurs, the upper-level (200 mb) jet core (winds ≥ 60 m s^{-1}) merges and extends eastward. This leads to increased zonal flow of wind and moisture and suggests that ARs that make landfall in SCA depend on the phase, position, and amplitude of the wave train.

Few studies have examined AR trajectories and lifecycles (e.g. Sodemann & Stohl 2013, Rutz et al. 2015, Ramos et al. 2016, Guan & Waliser 2019) and are often limited to singular case-study events (e.g. Moore et al. 2012). Only a select number of studies have examined overall ARs using trajectory models, such as Guan & Waliser (2019) who created a detection and tracking algorithm for global AR events. Other investigations of AR trajectories tend to be regional and are often focused on ARs that made landfall farther north along North America's western coast (e.g. Neiman et al. 2013). While use of trajectory models is often limited, these tools can provide us with valuable information about the characteristics of AR events in the days leading up to landfall. This research aims to examine the trajectories and lifecycles of ARs affecting the western coast of North America, with a focus on ARs affecting SCA. The main goal of this work is to determine the differences of SCA ARs from ARs that landfall farther north using trajectory locations and distances, as well as along-trajectory characteristics before and during landfall. This goal will be achieved by describing in detail the climatology of the trajectories and respective environmental conditions along the trajectories. The backward trajectory analysis is beneficial for this study as it provides hourly outputs of location as well as several along-trajectory characteristics important to AR progression, including pressure and specific humidity values, among others.

2. MATERIALS AND METHODS

Two gridded data sets from the National Centers for Environmental Prediction at the National Oceanic and Atmospheric Administration (NOAA) provide synoptic-scale conditions for these analyses: (1) the Climate Forecast System Reanalysis (CFSR), used for AR identification as well as determining AR landfall locations, and (2) the Global Data Assimilation System (GDAS), used for backward trajectories. We use daily CFSR (Saha et al. 2010) fields of total precipitable water (TPW) from 1979–2015 available at a 0.5° × 0.5° horizontal resolution and calculate daily anomaly fields at each grid point by removing the smoothed annual cycle. This data set was chosen for its horizontal resolution as well as daily availability. TPW (in kg m^{-2}) is an equivalent to integrated water vapor, which has been used in other detection algorithms (e.g. Wick et al. 2013), as it reflects the water total within an atmospheric column (vertically integrated, surface – 200 mb) if all water vapor condenses into liquid water with 1 kg m^{-2} equal to 1 mm (Campmany et al. 2010). We use daily GDAS (Kanamitsu 1989) analyses available from December 2004 until December 2015 at a 1.0° × 1.0° horizontal resolution with a vertical resolution of 25 hPa between 1000–900 hPa and 50 hPa between 900–50 hPa. This data set was chosen as it is already converted into a HYSPLIT-ready format, and is used in previous AR HYSPLIT analyses (e.g. Moore et al. 2012, Neiman et al. 2013).

We use a detection algorithm to identify ARs and their landfall locations for events affecting North America's west coast during the wet season months of October through March. This algorithm is based on an AR identification procedure by Jiang et al. (2014) with modifications outlined in Harris & Carvalho (2018). We use this algorithm as it captures events affecting the western coast of North America well (Harris & Carvalho 2018). The main input data for this algorithm is CFSR, and there are 5 main procedures. Steps 1 and 2 are based off the criteria of Jiang et al. (2014), whereas steps 3–5 are modifications. A brief explanation of each step follows with more detailed descriptions available in Harris & Carvalho (2018).

1. We scan TPW fields north (south) of 15.0° N (15.0° S) for contiguous regions with TPW grid points (Q_r) that meet the following criteria:

$$Q_r \geq Q_{z\text{mean}} + A(Q_{z\text{max}} - Q_{z\text{mean}}) \quad (1)$$

$$Q_r \geq Q_{m\text{mean}} + B(Q_{m\text{max}} - Q_{m\text{mean}}) \quad (2)$$

$$Q_r \geq q_{\text{cut}} = 20 \text{ mm} \quad (3)$$

where $Q_{z\text{mean}}$ and $Q_{z\text{max}}$ refer to the zonal (latitudinal, z) and $Q_{m\text{mean}}$ and $Q_{m\text{max}}$ refer to the meridional (longitudinal, m) mean and max. values of Q_r. Here, A (B) is 0.3 (0.1) and is meant to preserve the elongated shape of an AR. Finally, q_{cut} is a threshold value designating the minimum TPW value required to be an AR (Jiang et al. 2014).

2. To filter out regions that are too small to be ARs, we dismiss contiguous areas of $< 5.0 \times 10^5$ km^2.

3. We calculate each region's first 2 (orthogonal) eigenvectors (or principal components) by matching an ellipse that best fit the area and then interpreting the ellipse's 2 orthogonal axes as the eigenvectors. From these eigenvectors, we are able to determine eccentricity (defined as the ratio between the minor and major axes) and elongation. This approach is the primary difference between this algorithm and the one identified in Jiang et al. (2014).

4. Using the output of step 3, we filter out regions with eccentricities of >0.40 or with widths >1000 km. This captures the elongated and narrow structure of an AR (e.g. Zhu & Newell 1994, 1998, Ralph et al. 2005, 2006, Neiman et al. 2008a,b). To capture ARs within larger regions of TPW (such as an extratropical cyclone), we keep regions that have widths >1000 km if the eccentricity is also <0.30 to guarantee that even though the system is overall wide, that it is in fact elongated.

5. To capture ARs only affecting the western coast of North America, we calculate orientation of each region using the first eigenvector (PC-1). We determine how many degrees this eigenvector varies from the x-axis (counterclockwise) keeping those that range from 0.0–90.0°. This range is used as the dominant winds in this region are westerly.

We then designate ARs according into one of 3 landfall areas along the contiguous west coast of the USA with a domain of 32.0–49.0° N. As we are trying to differentiate between regions, we subdivide the domain into 3 latitudinally equal regions: SCA (32.0° ≤ latitude ≤ 37.0°), northern California (NCA; 33.0° ≤ latitude ≤ 43.0°), and Pacific Northwest (PNW; 44.0° ≤ latitude ≤ 49.0°). Each examined AR is an independent event identified as an AR with no other AR event within ±3 d of landfall. We then create backward air parcel trajectories of the AR events using the HYSPLIT model (Draxler & Hess 1997, 1998, Stein et al. 2015) from the Air Resources Laboratory at NOAA. HYSPLIT uses a Lagrangian methodology along with 3D meteorological fields of horizontal wind, temperature, pressure, and/or heights, along with surface pressure to create forward and backward trajectories. There are 159 independent AR

events (Table 1) identified through the algorithm that we examine through HYSPLIT. We chose not to examine AR events occurring with various phenomena including the Pacific/North American Teleconnection Pattern, Madden-Julian Oscillation (MJO), and El Niño–Southern Oscillation, because while overall AR activity may coincide with a particular phase of one phenomena (e.g. Payne & Magnusdottir 2014), a previous study by Harris & Carvalho (2018) determined no consistent relationship between any of these phenomena and AR landfall in a particular region along North America's west coast.

We use the TPW anomaly fields to determine locations of the maximum positive TPW anomaly overland for each AR event affecting the USA within 2.0° of the coastline. This is the main starting location (latitude, longitude), i.e. the first and center grid cell, for the backward trajectories. In HYSPLIT one backward trajectory is calculated from this grid cell. Additionally, we build a box of 8 other grid cells each offset by 1.0° longitude/latitude surrounding the original cell with a backward trajectory calculated at each cell to create a 3.0° latitude × 3.0° longitude box centered over the landfall location grid cell. This group of 9 cells/trajectories is obtained for each of the ending levels, 1000, 2000, and 3000 m above mean sea level (MSL), consistent with previous backward trajectories analyses of ARs using HYSPLIT (e.g. Moore et al. 2012) resulting in 27 calculated trajectories for each AR. Backward trajectories run hourly for the previous 72 h, consistent with Moore et al. (2012), with GDAS providing the 3D atmospheric conditions for the events including vertical motion fields. It is important to note that AR lifecycles range temporally. The designated 72 h is a framework to understand the selected AR events and their synoptic conditions. Longer or shorter temporal trajectories may be more appropriate depending on individual events. Since the main goal of this study is to provide a climatology of all AR events, we use 72 h as a guideline to evaluate properties that are consistent among ARs that landfall along the coastal western USA. Our analyses indicate that longer trajectories are subject to a number of distinct processes, increasing the variance among events (data not shown).

HYSPLIT computes trajectory advection using 3D velocity vectors (V) averages for initial, $P(t)$, as well as first guess, $P'(t + \Delta t)$, positions, where the advection distance per time step (Δt) is less than the grid spacing, and the velocity vectors are linearly interpolated in time and space. A preliminary explanation of the model along with its equations follows. Please see Draxler & Hess (1997) regarding HYSPLIT's construction and/or additional formulas used within the model. The first guess position is calculated as:

$$P'(t + \Delta t) = P(t) + V(P,t)\Delta t \quad (4)$$

and the final position is calculated as:

$$P'(t + \Delta t) = P(t) + 0.5[V(P,t) + (P',t + \Delta t)]\Delta t \quad (5)$$

HYSPLIT is terrain following (normalized σ coordinate) with

$$\sigma = (Z_{top} - Z_{msl})/(Z_{top} - Z_{gl}) \quad (6)$$

where Z_{top} is the height of the top of the model, Z_{msl} is the height of MSL, and Z_{gl} is the height of ground level, so that σ is normalized to be a fraction of the total model depth. If a trajectory leaves the top of the domain during the sequence, that trajectory is terminated, whereas if the trajectory contacts the ground during the run, it continues. When describing trajectories and along-trajectory characteristics, the term 'parcel' is sometimes used as a frame of reference for understanding environmental conditions during a trajectory, consistent with other HYSPLIT AR studies (e.g. Moore et al. 2012, Neiman et al. 2013). Parcels are best thought of as points with constant volumes following the course of the trajectory that do not interact with the environment.

Of the 159 ARs examined, only 30 make landfall in the SCA region, 70 in NCA, and 59 in PNW (Table 1). We find differences in trajectory distances as well as along-trajectory parcel measurements between the 3 landfall regions. Differences are most pronounced at the 1000 m MSL level although we also discuss the 2000 and 3000 m MSL levels when applicable. Figs. 1–5 depict variables at 1000 and 2000 m MSL only, as AR cores tend to occur below 2500 m, and various studies show the bulk of moisture flux around 1000 m (e.g. Ralph et al. 2005). We calculate differences be-

Table 1. Landfall regions, information, and numbers of identified landfalling atmospheric rivers (ARs) with backward trajectories calculated by means of HYSPLIT for Oct–Mar seasons from Dec 2004 to Dec 2015. Trajectory numbers are the number of individual trajectories calculated at each level

Name	Abbr.	Lat. covered (°N)	Landfalling ARs	Trajectories per level
Pacific Northwest	PNW	44.0–49.0°	59	531
Northern California	NCA	38.0–43.0°	70	630
Southern California	SCA	32.0–37.0°	30	270
All ARs	–	32.0–49.0°	159	1431

tween landfall area groups using a sign-test (Anderson & Finn 1996), which compares the distributions of 2 groups based on medians. The sign-test involves merging together the 2 groups of interest, determining the median of the combined group (M), and then using a 2 proportion *Z*-test calculated as:

$$z = \frac{\hat{p}_1 - \hat{p}_2}{\sqrt{\hat{p}\hat{q}\left(\frac{1}{n_1} + \frac{1}{n_2}\right)}} \quad (7)$$

where $\hat{p}_1$ ($\hat{p}_2$) is the proportion of the first (second) sample group that is greater than M from the combined group. Value $\hat{p}$ ($\hat{q}$) is the proportion of the combined group that is greater (less) than M (as M is the median value of the combined group, by definition these proportions must be ½ and ½), with n_1 (n_2) as the number in the first (second) sample group. The test is 2-tailed with larger z values indicating distributions that have greater differences from one another with critical values of ±1.96 at the 95% (α = 0.05) significance level (Anderson & Finn 1996).

3. HYSPLIT RESULTS

3.1. Trajectory pathways and distances

We calculate median geographic trajectory locations along with interquartile ranges (IQRs) for all ARs that make landfall within specified regions to determine the overall movements of these events as well as to discern any differences in AR behavior between landfall regions. The IQRs help to discern where the bulk of trajectory locations for a specific region occur. For trajectories ending at 1000 m MSL (Fig. 1), median trajectories for all regions are quasi-zonal and exhibit cyclonic curvature. Trajectories become less zonal with less cyclonic curvature at 2000 m (Fig. 1) and 3000 m MSL (data not shown) and extend in a northeastward direction. Qualitatively, ARs that make landfall farther south appear to have the most cyclonic curvature at 1000 m MSL, although they display the most 'zonal' orientations at 2000 m MSL, which is consistent with a previous North American AR study by Harris & Carvalho (2018). SCA AR trajectory locations 72 h before landfall are, as expected, farther eastward as well as farther south than comparable trajectories of ARs that make landfall farther north (Harris & Carvalho 2018). Over the course of 72 h, all SCA trajectories remain north of 25.0° N with only a few trajectories in the 25th quartile traveling south of 30.0° N. As moisture within an AR is from a combination of local sources, such as convergence along a cold front, as well as from horizontal transport

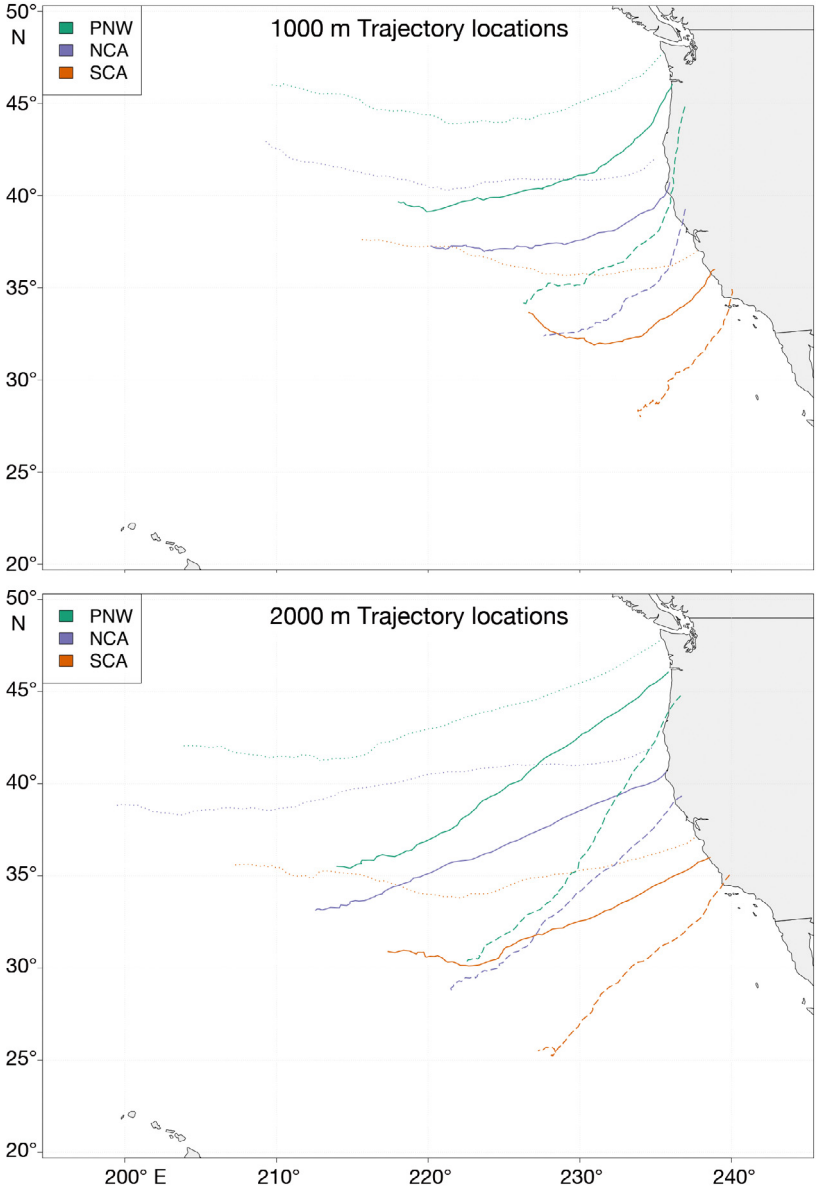

Fig. 1. Median (solid lines), 25th (dashed lines), and 75th (dotted lines) quartile trajectories over 72 h according to landfall region and level; see Table 1 for region abbreviations

of moisture over distances (Bao et al. 2006), this suggests that moisture sources for many of these events may not be tropical in nature within 72 h of landfall. Additionally, it suggests that AR manifestation and moisture sources may vary according to landfall region.

At all levels, SCA ARs have the shortest median trajectories but the IQR indicates that trajectory distances vary (Table 2). For trajectories ending at 1000 m MSL, SCA AR trajectories are significantly shorter than both NCA and PNW ARs but they have the highest IQR. At 2000 m MSL, SCA ARs are significantly shorter than NCA ARs with similar dispersions. For trajectories ending at 3000 m MSL, SCA, NCA, and PNW ARs are not significantly different from one another, although SCA ARs still have the shortest median trajectories. Since over the course of 72 h SCA ARs do not travel as far as their northern counterparts, they are slower moving. As ARs are often related to extratropical cyclones (Bao et al. 2006, Dettinger et al. 2015, Gimeno et al. 2016), these differences in speeds may imply that some extratropical cyclones are not likely to affect SCA ARs in the same manner as NCA and PNW ARs. For example, SCA ARs may tend to be more stationary; thus, several extratropical cyclones may affect a single SCA AR event such as with the case study event discussed in Section 4. Another possibility is the impact of regional topography on landfalling ARs. Topographical changes in SCA are significant and regions with high topography may slow down AR progression across a landscape (Wang et al. 2019).

3.2. Along-trajectory characteristics

We calculate the medians and IQRs of along-trajectory values for all ARs that make landfall within specified regions to gain insight into the conditions present during AR progression. All trajectories ending at 1000 and 2000 m MSL experience either some parcel moistening (1–3 g kg^{-1}) or moisture holds constant (Fig. 2), except for the hours directly before (0–15 h) landfall. Moistening tends to occur at higher rates in the earlier trajectory hours, farther from landfall. Additionally, at all levels most trajectories experience subsidence (≤1.75 hPa h^{-1}) before landfall (Fig. 3) (15–72 h). This increase in moisture along with subsidence can be explained by either evaporation (e.g. from the

Table 2. Median and interquartile range (IQR; 25th–75th percentile) distances (km) of backward trajectories according to level and region (see Table 1 for region abbreviations)

Level	Region	Median	IQR
1000 m	PNW	2497.10	1131.29
	NCA	2328.45	1233.11
	SCA	1877.79	1275.58
2000 m	PNW	2955.83	1296.97
	NCA	2897.58	1423.41
	SCA	2625.03	1420.74
3000 m	PNW	3497.14	1601.92
	NCA	3588.85	1886.13
	SCA	3324.98	2220.24

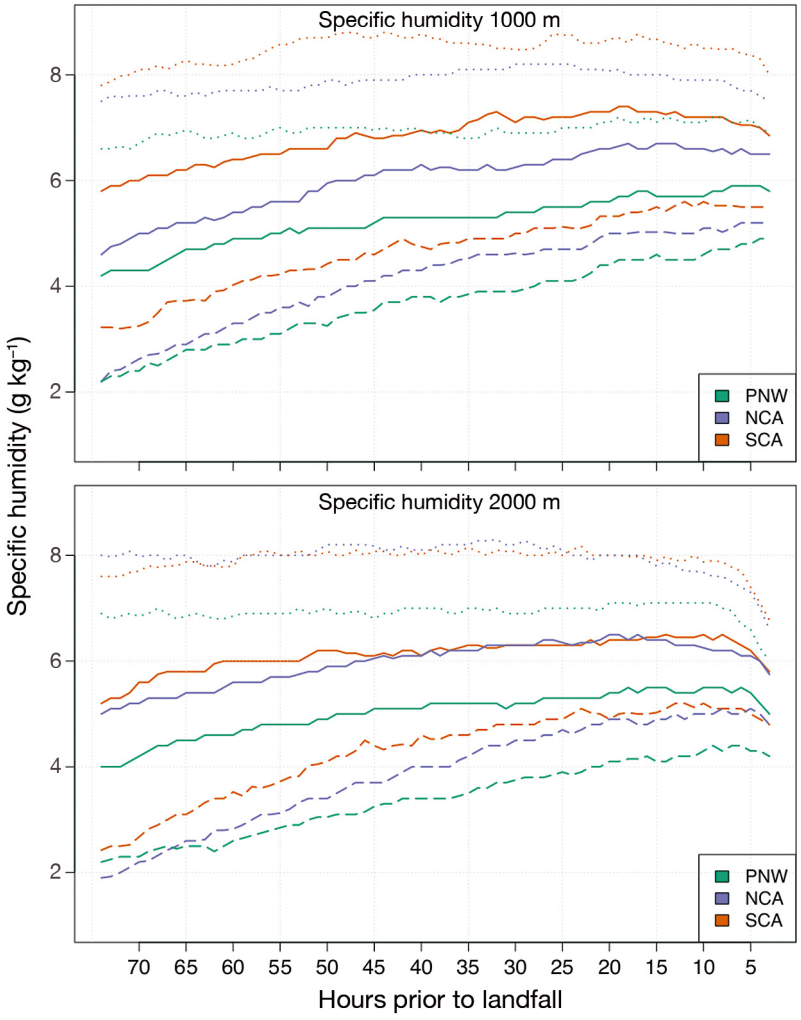

Fig. 2. Time series of median (solid lines), 25th (dashed lines), and 75th (dotted lines) quartile values of hourly specific humidity according to landfall region and level; see Table 1 for region abbreviations

ocean surface or from precipitation) or moisture advection by the winds (Trenberth 1999). With temperatures (Fig. 4), for parcels ending at 1000 m MSL we see warming (1–3 K) over the course of the trajectory, most likely due to subsidence (Fig. 3), whereas at 2000 m MSL temperatures stay near constant until the hours before landfall. Additionally, we see a gradual rise of relative humidity (Fig. 5) over the course of the trajectories. Towards landfall for all regions, specific humidity levels drop and air rises with corresponding drops in temperature as well as rises in relative humidity values to greater than 70%, indicating orographic uplift resulting in condensation and precipitation.

There are differences in along-trajectory measurements of temperature and specific humidity between different landfall regions. For parcels ending at 1000 m MSL, the maximum temperatures recorded along trajectories (t_{max}) are significantly higher with a smaller IQR for SCA than either NCA or PNW ARs (Table 3). For trajectories ending at 2000 m MSL, there are no statistically significant differences in t_{max} values between SCA and NCA ARs, although both SCA and NCA ARs are significantly warmer than PNW ARs. Again, SCA ARs have the smallest IQR. SCA ARs show no significant differences from either NCA or PNW for trajectories ending at 3000 m MSL. This signifies that at lower levels, SCA ARs tend to reach temperatures that are warmer than both NCA and PNW ARs, and that temperatures vary the least but that these differences are most pronounced lower in the atmosphere and diminish higher up.

SCA ARs also have significantly higher temperatures recorded at landfall (t_{land}) at both 1000 and 2000 m MSL compared to both NCA and PNW (Table 3). At both levels, NCA ARs are also significantly warmer than PNW ARs for both t_{max} and t_{land}. For trajectories ending at 3000 m MSL, SCA ARs are still the warmest at landfall although they do not vary significantly from NCA ARs. Both SCA and NCA ARs vary significantly from PNW ARs. At all levels, SCA ARs median t_{land} values do not drop below freezing (273.15 K), and at 1000 m MSL, SCA ARs have no t_{land} values below freezing.

To understand changes of along-trajectory characteristics, we calculate differences between each trajectory's maximum measurement and their respective landfall measurement (i.e. delta = max. – land). With the differences in temperature (t_{delta}), at 1000 m MSL statistically significant differences exist between SCA and NCA ARs as well as NCA and PNW ARs but not between SCA and PNW ARs (Table 3). At 2000 and 3000 m MSL, t_{delta} for SCA, NCA, and PNW ARs are not significantly different. This indicates that SCA and PNW ARs at 1000 m MSL experience less cooling over the course of their trajectories than NCA ARs, which experience more cooling. For trajectories ending at 2000 and 3000 m MSL, all ARs regardless of landfall location experience similar temperature changes.

These results are somewhat as expected, as SCA is closer to the equator and the environment in which ARs evolve is generally warmer. This increase in

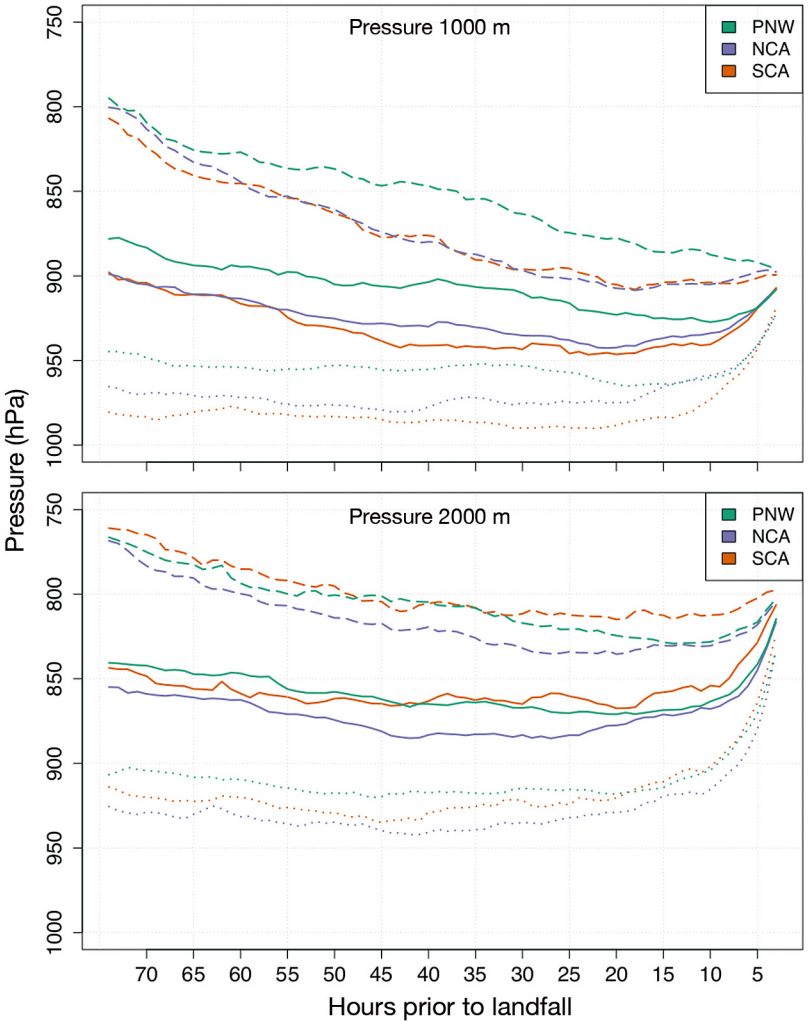

Fig. 3. Same as Fig. 2, but for pressure

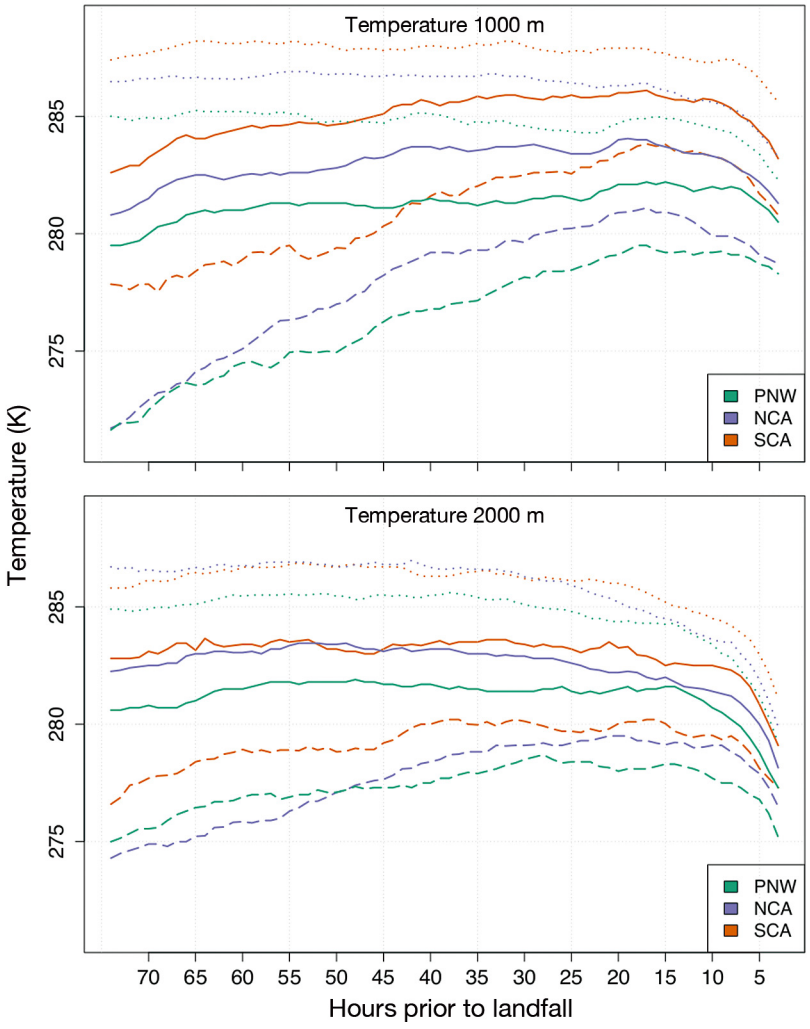

Fig. 4. Same as Fig. 2, but for temperature

temperature with decrease in latitude as well as the lower cooling values are also indicators that SCA ARs are more likely to originate/travel through warmer latitudes. Furthermore, these warmer temperatures indicate events with conditions that are more likely to lead to liquid precipitation rather than snow at least upon initial landfall. This will vary upon inland intrusion as well as interactions with topographical barriers and resulting orographic uplift. While AR-induced events with temperatures below the freezing temperature of 273.15 K are more common farther north and provide integral inputs to water budgets (e.g. Guan et al. 2013), warmer ARs have been linked to several extreme events resulting in flash flooding (e.g. Ralph et al. 2006) throughout much of the US west coast.

Concerning specific humidity, differences between regions are most prominent for trajectories ending at 1000 m MSL. SCA ARs at this level have significantly higher maximum along-trajectory specific humidities (q_{max}) (Table 3) as well as specific humidities at landfall (q_{land}) (Table 3) than both NCA and PNW ARs. At 2000 and 3000 m MSL, SCA and NCA ARs have significantly higher q_{max} values than PNW ARs, but SCA and NCA ARs are comparable to one another. For q_{land} at 2000 m MSL, SCA and NCA have significantly higher values than PNW but do not differ from one another. At 3000 m MSL, all 3 regions vary significantly from one another, although NCA has the highest q_{land} values. With the differences of maximum and landfall specific humidity values along trajectories (i.e. $q_{delta} = q_{max} - q_{land}$), for trajectories ending at 1000 m MSL, SCA ARs have the highest median values and IQR but are only statistically different from PNW ARs (Table 9). There are no significant differences in q_{delta} between regions at 2000 m MSL. At 3000 m MSL, SCA and NCA are significantly different than PNW but not from one another.

Similar to temperature, along-trajectory measurements of specific humidity show the most prominent differences lower in the atmosphere. As SCA ARs often have higher q_{max} and q_{land} values compared to NCA and PNW ARs, they are capable of transporting large amounts of moisture. These higher moisture values may be partially explained by the corresponding higher temperatures discussed previously, as warmer temperatures increase water's equilibrium vapor pressure. Also, at lower altitudes SCA ARs experience the greatest losses of moisture along their trajectories (q_{delta}), which may be indicative of the influence of high topography and orographic forcing on these events. Higher in the atmosphere, regardless of landfall region, ARs experience similar moisture losses along the course of their trajectories.

In an attempt to differentiate the atmospheric characteristics of SCA AR events compared to ARs which made landfall farther north, we create day of landfall composites using additional CFSR fields for each landfall region. To determine if events with high specific humidity values differ in their atmospheric qualities, composites are created for events exceeding the

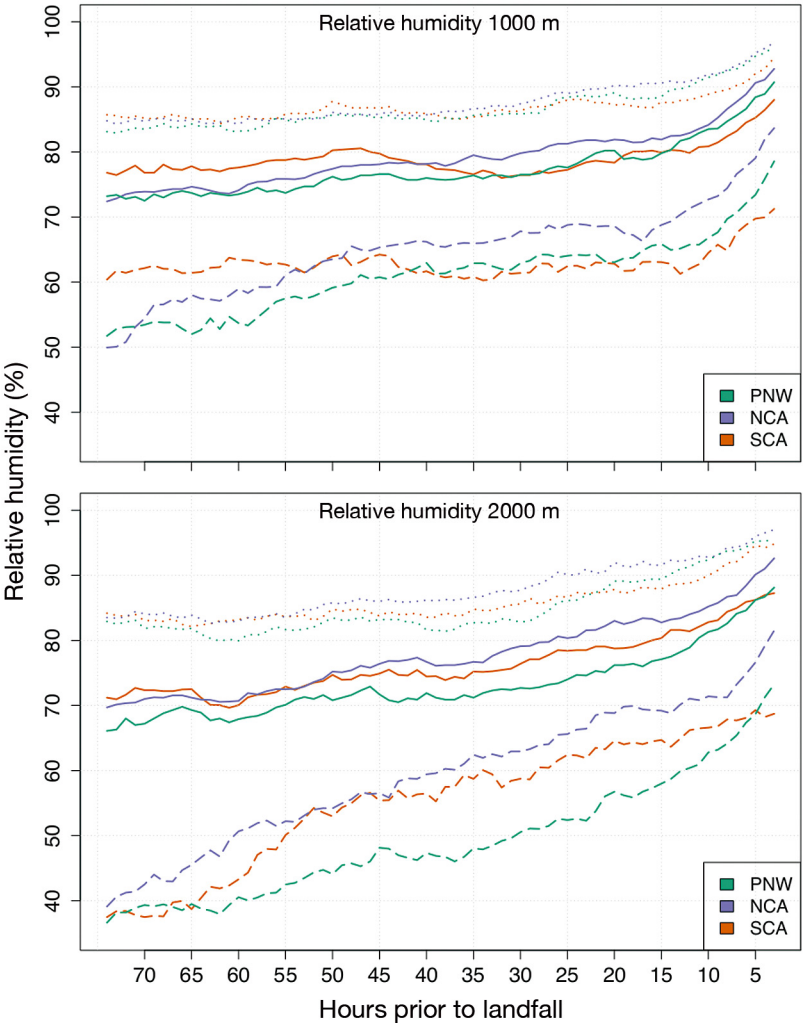

Fig. 5. Same as Fig. 2, but for relative humidity

75th percentile for both q_{max} and q_{land} at 1000 and 2000 m MSL. Fig. 6 show composites for events exceeding the q_{land} 75th percentile for trajectories ending at 1000 m MSL. Composites for events exceeding the q_{max} 75th percentile (data not shown) as well as trajectories ending at 2000 m MSL (data not shown) show similar results.

Overall, for all regions, on the day of landfall there is a plume of enhanced TPW (≥20 mm) extending to the coast from lower latitudes, between areas of low and high sea level pressure (SLP) (Fig. 6). There is an offshore trough and onshore ridge with strong winds funneling moisture towards the coast. Yet for SCA ARs, there is a continuous track of higher (≥25 mm) TPW values extending from south of 30.0° N compared to ARs that make landfall farther north which have lower and/or discontinuous TPW values. Along with a weaker SLP gradient and a shallow onshore trough, there is increased zonal flow for SCA ARs, whereas the SLP gradient is strongest and the onshore ridge most amplified for PNW ARs. All this is consistent with the median AR trajectory orientations discussed earlier (Fig. 1).

4. CASE STUDY ANALYSIS

In this section, we describe a powerful AR event to affect SCA on 17 February 2017 (021717). After years of persistent drought, the 2016–2017 water season brought significant precipitation to California. The 021717 event was a well-forecasted AR that initially made landfall in NCA. We chose to analyze this particular AR since by the time of landfall in SCA it had strengthened from initial forecasts. This event delivered torrential rainfall and strong winds to several coastal SCA cities including Santa Barbara, Ventura, and Los Angeles, leading to flooding of low-lying areas as well as tree and structural damage, costing the state millions in reported repairs[1]. Additionally, this event occurred during a period of enhanced MJO activity according to NOAA's Climate Prediction Center[2]. A few days before 021717, the MJO was in phase eight[2], with the MJO signal evident in the central Pacific Ocean and into the Western Hemisphere (Zhang 2005). MJO activity is linked to high-intensity rainfall values throughout the western coast of North America (Jones & Carvalho 2012). Also, Payne & Magnusdottir (2014) concluded that higher frequencies of landfalling ARs to North America's west coast occur during phase 8 of the MJO.

We use previously described CFSR reanalysis fields to examine the synoptic conditions on the day of and in the hours leading up to 021717's landfall. We also use Global Precipitation Mission (GPM) data from NASA to illustrate the event's rainfall. Specifically, we use 30 min Integrated Multi-satel-

[1] www.fortune.com/2017/02/25/california-storm-damage-costs

[2] www.cpc.ncep.noaa.gov/products/precip/CWlink/MJO/ARCHIVE/PDF/mjo_evol-status-fcsts-20170220.pdf

Table 3. Median, interquartile range (IQR; 25th–75th percentile), minimum (Min.) and maximum (Max.) maximum along-trajectory temperature (t_{max}), landfall temperatures (t_{land}), differences of temperature (t_{delta}), maximum specific humidity (q_{max}), landfall specific humidity (q_{land}) and differences of specific humidity (q_{delta}) of backward trajectories according to level and region (see Table 1 for region abbreviations)

Level	Region	Median	IQR	Min.	Max.
t_{max} (K)					
1000 m	PNW	285.0	5.6	273.1	296.9
	NCA	286.3	5.6	273.3	296.8
	SCA	288.1	4.8	275.9	300.9
2000 m	PNW	284.5	5.8	271.3	296.1
	NCA	285.9	6.5	271.7	299.4
	SCA	286.4	5.1	272.2	299.5
3000 m	PNW	283.4	6.7	265.5	297.8
	NCA	285.3	8.2	267.8	297.7
	SCA	284.9	8.3	270.5	296.0
t_{land} (K)					
1000 m	PNW	280.5	4.0	269.8	287.8
	NCA	281.3	4.6	265.5	286.9
	SCA	283.2	4.8	274.1	293.2
2000 m	PNW	277.3	4.0	260.6	286.2
	NCA	278.2	3.4	269.2	284.6
	SCA	279.1	3.8	271.3	291.1
3000 m	PNW	272.9	4.1	262.6	281.9
	NCA	274.0	3.3	266.8	280.9
	SCA	274.3	3.6	267.6	285.6
t_{delta} (K)					
1000 m	PNW	4.2	4.2	0.0	15.8
	NCA	4.6	4.6	0.0	19.5
	SCA	4.1	4.3	0.0	13.4
2000 m	PNW	7.0	4.7	0.0	22.1
	NCA	7.2	5.3	0.0	21.2
	SCA	6.9	5.6	0.0	19.0
3000 m	PNW	10.7	6.5	0.4	26.4
	NCA	11.1	7.1	0.0	25.0
	SCA	10.2	8.6	0.0	23.1

Level	Region	Median	IQR	Min.	Max.
q_{max} (g kg^{-1})					
1000 m	PNW	6.9	2.7	2.8	14.0
	NCA	7.7	2.9	1.5	14.5
	SCA	8.4	3.0	1.9	13.9
2000 m	PNW	6.7	3.2	1.7	15.0
	NCA	7.7	3.4	1.5	15.0
	SCA	7.8	3.1	2.0	14.5
3000 m	PNW	5.6	4.3	0.7	15.1
	NCA	7.1	5.0	0.8	15.8
	SCA	7.0	4.9	1.7	15.3
q_{land} (g kg^{-1})					
1000 m	PNW	5.8	2.0	2.0	9.8
	NCA	6.5	2.3	1.4	10.2
	SCA	6.9	2.5	1.4	10.4
2000 m	PNW	5.0	1.8	1.6	9.5
	NCA	5.8	1.8	1.3	9.3
	SCA	5.8	2.0	1.4	8.6
3000 m	PNW	4.1	1.7	0.6	8.4
	NCA	4.7	1.6	0.6	8.1
	SCA	4.4	1.8	1.0	6.6
q_{delta} (g kg^{-1})					
1000 m	PNW	0.8	1.5	0.0	5.8
	NCA	0.9	1.6	0.0	6.9
	SCA	1.0	2.0	0.0	10.2
2000 m	PNW	1.5	2.2	0.0	7.0
	NCA	1.7	2.4	0.0	7.6
	SCA	1.7	2.5	0.0	7.0
3000 m	PNW	1.6	3.0	0.0	9.7
	NCA	2.2	4.0	0.0	11.1
	SCA	2.6	4.1	0.0	11.6

litE Retrievals for GPM (IMERG) available on a 0.1° × 0.1° spatial resolution spanning 60.0° N–S. IMERG is a multi-satellite algorithm that uses estimates computed from various passive microwave sensors combined with microwave geo-IR fields that are then modified with monthly rain gauge surface data (Huffman et al. 2017). More information about IMERG can be found in Huffman et al. (2017). We use HYSPLIT to create backward trajectories for this event to determine how this AR compares to average SCA ARs. Like before, we force HYSPLIT with 1.0° GDAS, calculating 72 h backward trajectories at hourly intervals ending on 021717 18:00 h UTC. We choose 18:00 h UTC as this hour aligns well with the precipitation and synoptic conditions discussed below. We calculate 9 backward trajectories at each level for 3 levels: 1000, 2000, and 3000 m MSL.

4.1. Synoptic conditions

IMERG precipitation data for 021717 18:00 h UTC (Fig. 7) depicts light precipitation values (≤5 mm) throughout California including areas offshore. Rainfall corresponds to a comma formation typical to extratropical cyclones. A narrow band of high precipitation (≥11 mm) occurs ahead of the presumed cold front location, impinging on the Santa Ynez Mountains. This area of strong rainfall is associated with the defined AR event, consistent with Dettinger et al. (2015) and Eiras-Barca et al. (2018) who stated that AR moisture transport related to extratropical cyclones occurs in the pre-cold frontal area and is separate as well as distinct from precipitation within the warm conveyor belt area closest to the center of the extratropical cyclone. These narrow bands of moisture and subsequent precipitation reach a max-

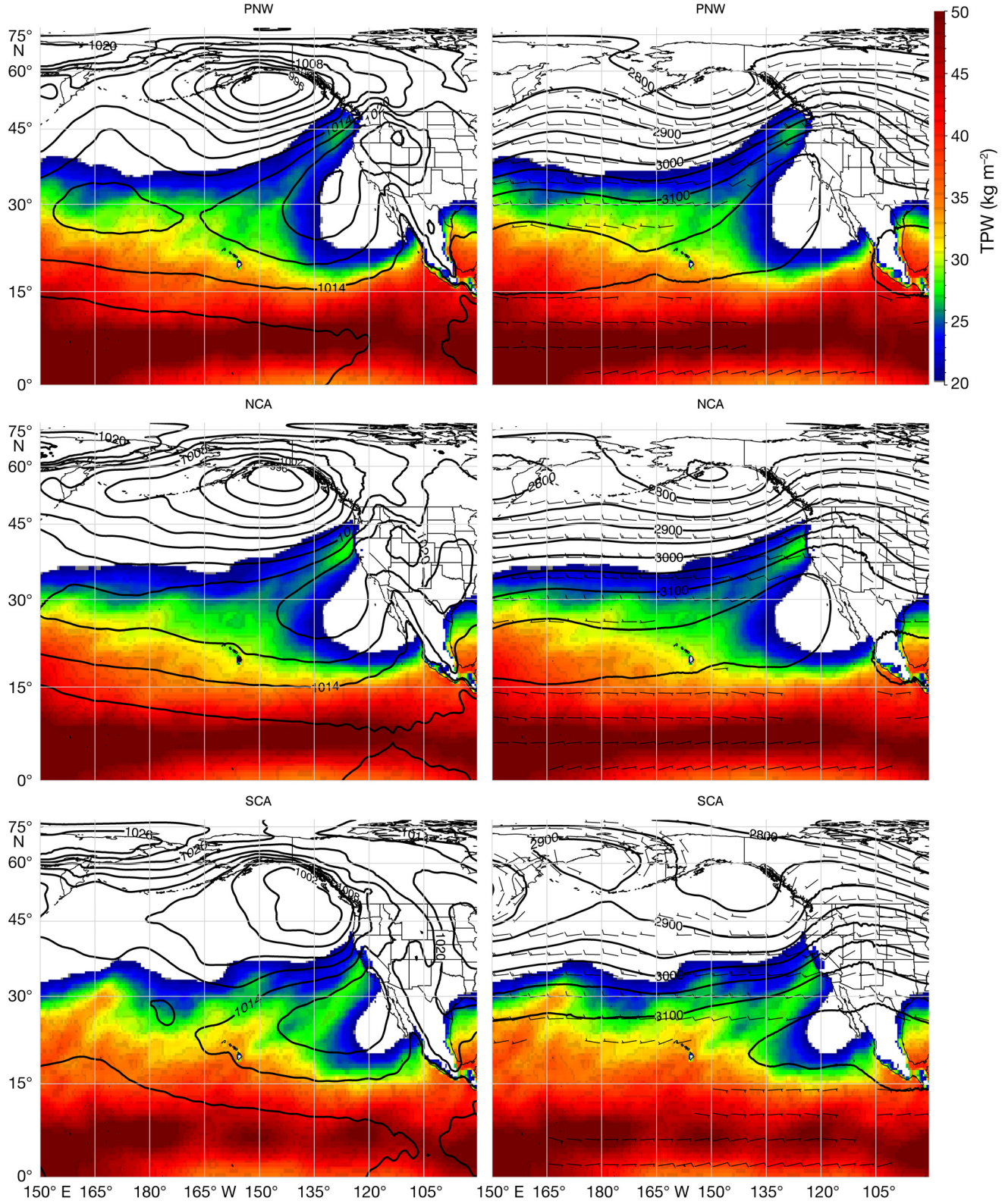

Fig. 6. Composite atmospheric conditions for atmospheric river landfall days according to landfall region (see Table 1 for region abbreviations). (Left) Sea level pressure (hPa) (contours) and total precipitable water (TPW) (fill); (Right) 700 mb geopotential heights (gpm) (contours), TPW (fill), and winds (m s^{-1}) (barbs). Note that the minimum value for total precipitable water is 20 and wind is 5, with smaller values not shown

imum if an AR encounters an orographic barrier such as a mountain range (Eiras-Barca et al. 2018) as seen with this AR and the Santa Ynez Mountains.

CFSR fields (Fig. 8) on 16 February 2017 (021617) 06:00 h UTC depict a corridor of strong westerly/southwesterly 850 mb flow associated with a low-pressure system offshore from North America's Pacific northwest coast at around 49.0° N and a corresponding TPW plume with values ≥20 mm extending from the Hawaiian Islands (~20.0° N, ~155.0° W) to ~38.0–42.0° N along the western coast. At 500 mb there is a wide offshore trough along with vorticity maximums offshore between ~40.0–50.0° N. There are strong geopotential height gradients between both offshore troughs and onshore ridges at 850 and 500 mb. After initial AR landfall, TPW values migrate southward and weaken along with winds. This southeastward progression is consistent with Wang et al.'s (2019) analysis of other ARs that made landfall in SCA. By 18:00 h UTC on 021617 we see the development of a frontal wave at 850 mb. This wave strengthens at 06:00 and 18:00 h UTC on 021717 and develops into a low-pressure system which can be seen in both geopotential height as well as absolute vorticity fields. This mesoscale frontal wave and development of a second low-pressure system are the primary reasons for this storm's high intensity and leads to the shifting in the offshore trough's axes, encouraging movement of strong wind and moisture towards SCA which allows for the augmentation of TPW seen at 06:00 h UTC on 021717 due to increased convergence along the cold front (e.g. Bao et al. 2006). This is not the first time an AR has been strengthened by its interactions with a mesoscale frontal wave. Ralph et al. (2011) describes an event that occurred in the Pacific Northwest in March 2005 where a frontal wave increased the duration of an AR's conditions at landfall for a particularly strong and damaging event.

4.2. HYSPLIT analysis

For the variations of geographic trajectory location and temporal along-trajectory characteristics, we use the medians of the 9 trajectories at each level. According to this case study's temporal characteristics (Fig. 9a–d), trajectories ending at each level are mostly consistent with the temporal characteristics for regions examined earlier. There are decreases in pressure (Fig. 9a) ~12 h before and during landfall for all 3 levels along with increases of relative humidity (Fig. 9b) with values reaching over 90%, decreases of temperature (Fig. 9c), and increases of specific humidity (Fig. 9d), which are all consistent with orographic uplift and subsequent precipitation. In the 72 h before landfall, pressure remains relatively constant, whereas in the regional temporal averages there is an increase of pressure indicative of subsidence. The trajectories ending at 1000 m MSL remain close to the sea surface until lifting begins, while trajectories ending at 2000 and 3000 m MSL remain at low altitudes (>900 hPa) until lift. Relative humidity is high (>75%) in the hours before landfall with increases in relative humidity towards landfall. Temperatures before landfall stay relatively constant at each level. For specific humidity, at 1000 and 2000 m MSL there are increases over the course of the trajectory, but at 3000 m MSL specific humidity decreases.

Overall, this AR has much higher specific humidity values and slightly higher temperatures than the previously examined ARs, including those that made landfall in SCA. In terms of q_{max} (Fig. 10), this event has higher median values (9.8 g kg^{-1} at 1000 m MSL,

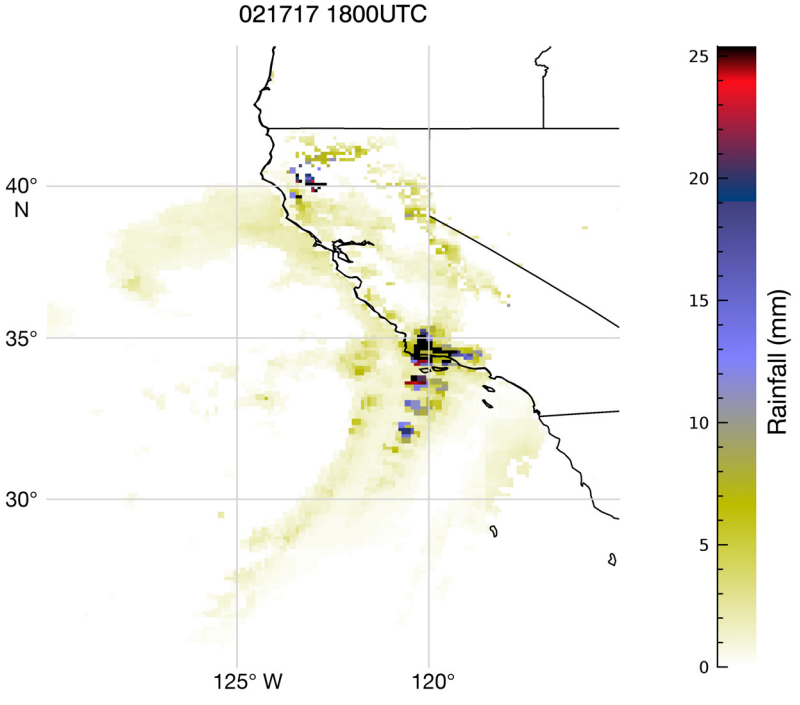

Fig. 7. Gridded (0.1° × 0.1°) global precipitation measurement rainfall data (in mm) for the 021717 (17th February 2017) case study event at 18:00 h UTC

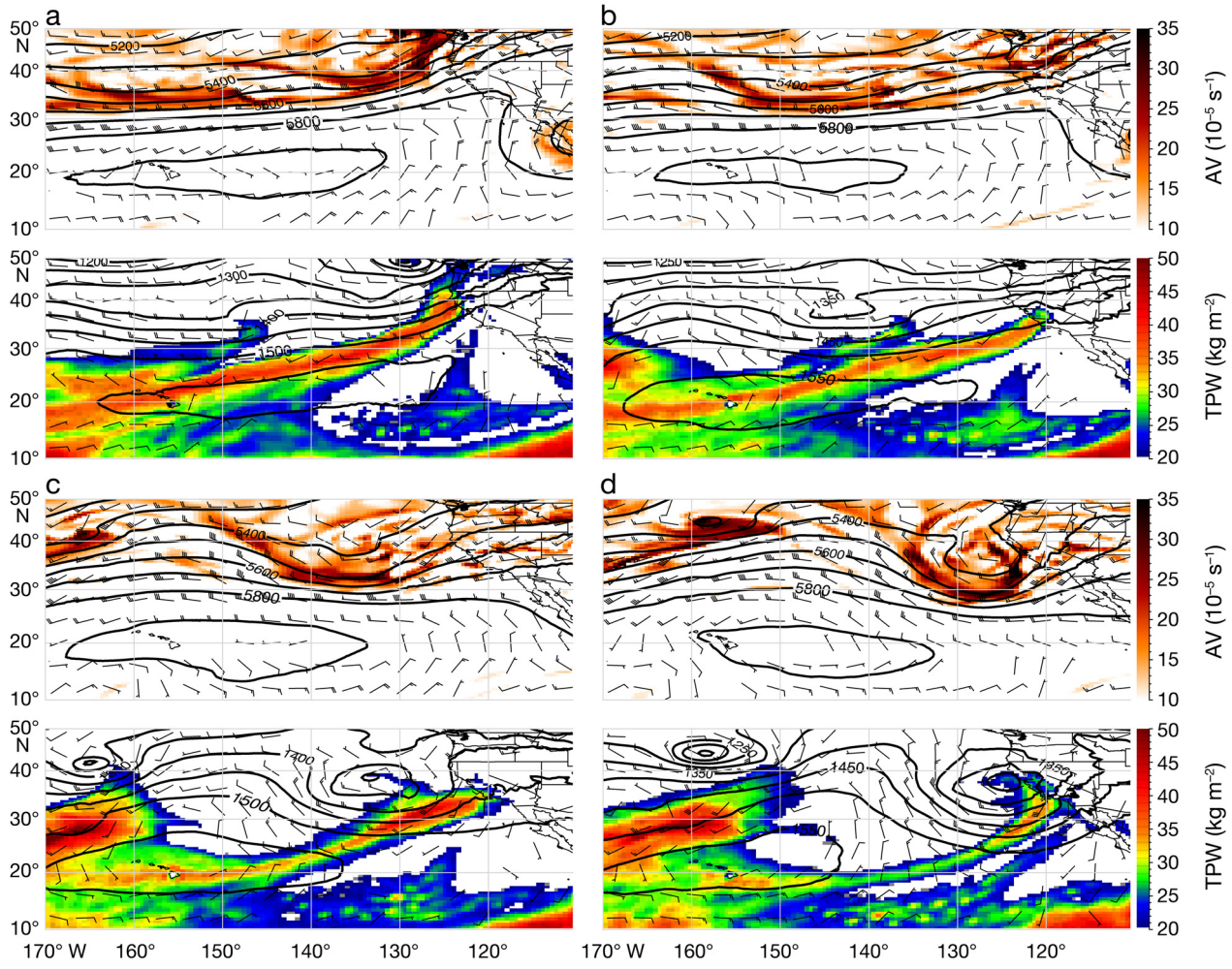

Fig. 8. Atmospheric conditions for the 021717 case study event from reanalysis. Each figure consists of 2 images: (top) 500 mb geopotential heights (gpm) (contours), absolute vorticity (AV) (fill), and winds (m s^{-1}) (barbs); (bottom) 850 mb geopotential heights (contours), total precipitable water (TPW) (fill), and winds (barbs). Note that the minimum value for absolute vorticity is 10, wind is 5, and TPW is 20, with smaller values not shown. Observed times are: (a) 021617 (16th February 2017) 06:00 h UTC; (b) 021617 18:00 h; (c) 021717 (17th February 2017) 06:00 h; and (d) 021717 18:00 h

8.9 g kg^{-1} at 2000 m MSL, and 9.7 g kg^{-1} at 3000 m MSL) at all levels than all regional ARs, with values surpassing SCA's 75th percentile for q_{max} moisture at 1000 and 3000 m MSL. An analysis of CFSR reveals that the climatological mean specific humidity values during February (1979–2015) for (ocean) grid cells between 220.0–240.0° E and 20.0–35.0° N is 6.6 g kg^{-1} at 925 mb, 3.6 g kg^{-1} at 850 mb, and 1.8 g kg^{-1} at 700 mb (data not shown). Thus, specific humidity for this event was far above regional moisture averages for the season. At all levels this AR has the highest q_{land} values (Fig. 10) (q_{land} medians: at 1000 m MSL, 8.1 g kg^{-1}; 2000 m MSL, 7.1 g kg^{-1}; and 3000 m MSL, 5.7 g kg^{-1}) and surpasses the 75th percentile for q_{land} measured moisture for SCA ARs at all levels as well. Additionally, this AR also has higher t_{max} values (Fig. 11) (medians: at 1000 m MSL, 290.2 K; 2000 m MSL, 287.3 K; and 3000 m MSL, 289.1 K) at all levels but, median t_{land} temperature values (Fig. 11) (medians: at 1000 m MSL, 283.5 K; 2000 m MSL, 280.7 K; and 3000 m MSL, 276.6 K) are comparable to other SCA ARs (Table 3). This may be due to this event originating from much lower in the troposphere (Fig. 9a) and, unlike regional averages, these trajectories do not experience long-duration subsidence. These very high specific humidity values and high temperatures may partially account for the high-intensity rainfall (Fig. 8) seen during this event. We also see that over the course of 72 h these trajectories have shorter trans-Pacific pathways (Fig. 12), indicating a very slow-moving system, but are consistent with previous results in that 1000 m MSL

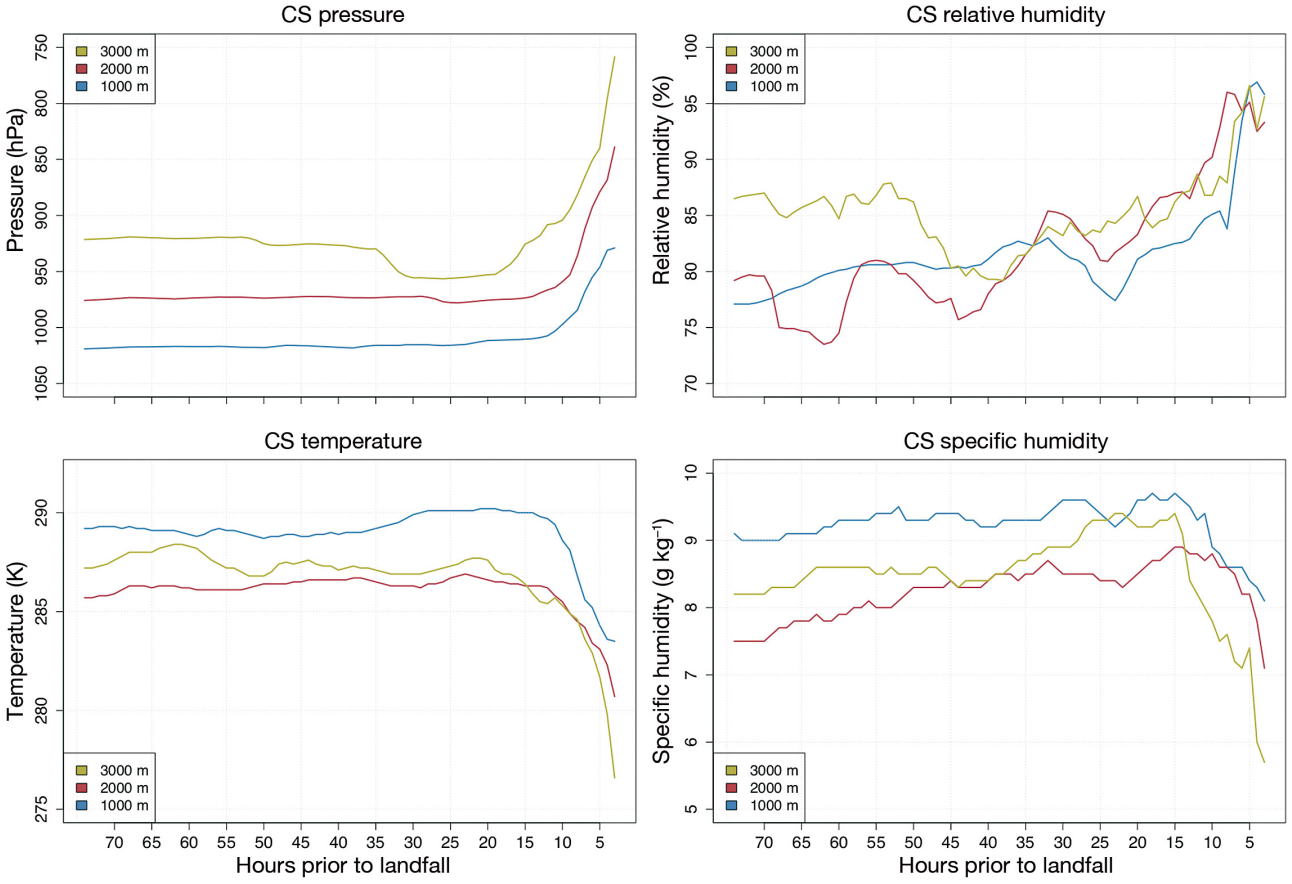

Fig. 9. Hourly time series of median along-trajectory values for the 021717 (17th February 2017) case study event according to landfall level. Observed characteristics include (a) pressure; (b) relative humidity; (c) temperature; and (d) specific humidity

(median: 1282.85 km) trajectories are the shortest, followed by 2000 m (median: 1478.51 km), and then 3000 m MSL (median: 2122.66 km) trajectories (Fig. 13). Although in the 72 h before landfall, these trajectories travel from south of 30.0° N, indicating more tropical sources of moisture and high overall temperatures.

5. CONCLUSIONS

We use a Lagrangian backward trajectories model (HYSPLIT) to compute backward trajectories of 159 ARs that make landfall along the US west coast from December 2004 to December 2015 for the hour of landfall and hourly for 72 h before landfall. We then compare SCA ARs to ARs that make landfall farther north. One-degree GDAS data is used to force HYSPLIT with 3D atmospheric variables. Nine trajectories are modeled at each of the 3 ending atmospheric levels, 1000, 2000, and 3000 m MSL, for a total of 27

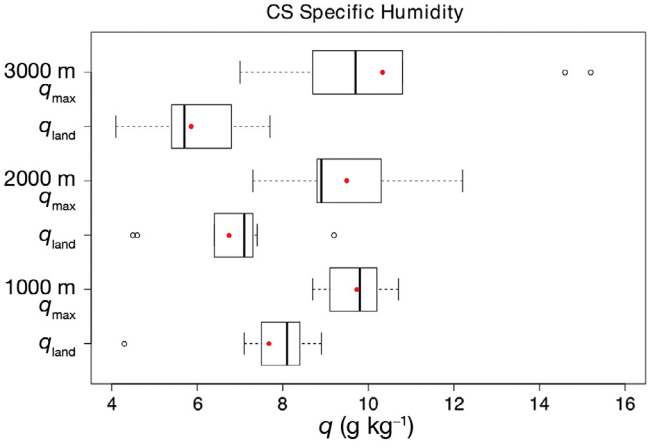

Fig. 10. Boxplots of trajectory maximum (q_{max}) and landfall (q_{land}) specific humidity values for the 021717 (17th February 2017) case study (CS) event according to landfall level. Box depicts interquartile range (IQR) (25th–75th percentile), whiskers depict values within 1.5× IQR of the IQR with median (black lines) and mean (red dots) values. Outliers are depicted as open circles

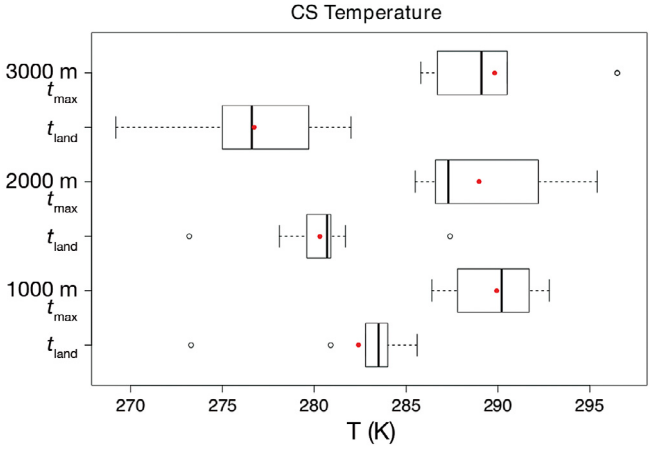

Fig. 11. Same as Fig. 10, but for maximum (t_{max}) and landfall (t_{land}) temperatures

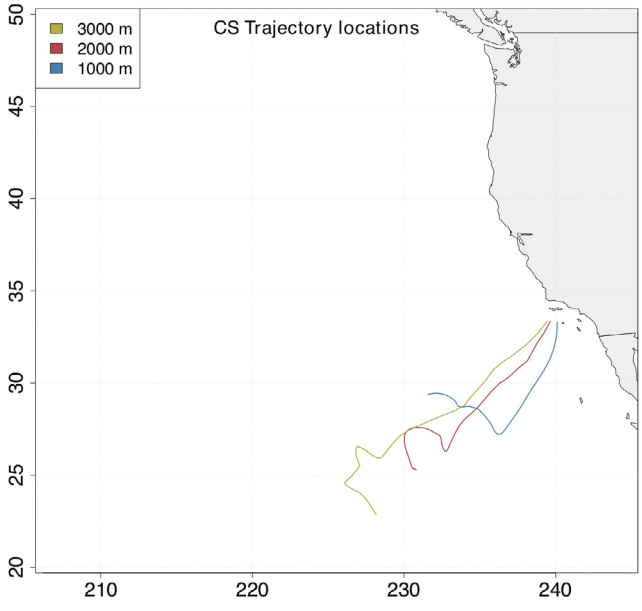

Fig. 12. Median trajectories over 72 h for the 021717 (17th February 2017) case study event according to landfall level

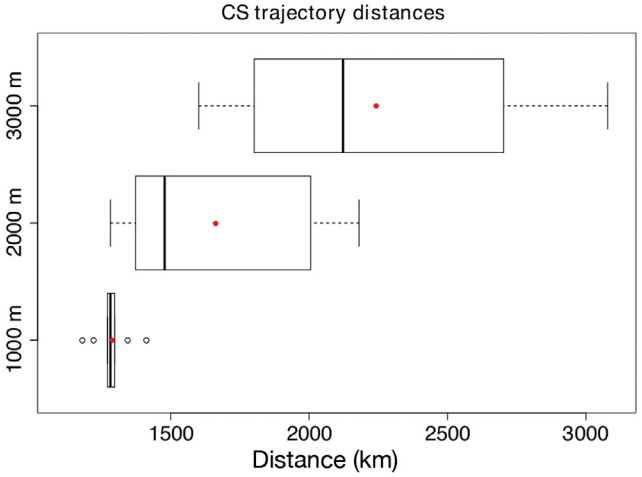

Fig. 13. Atmospheric river trajectory distances for the 021717 (17th February 2017) case study (CS) event according to landfall level. Box and whiskers depict interquartile range with median (black lines) and mean (red dots) distances. Outliers are depicted as open circles

backward trajectories calculated for each AR. In the 72 h before landfall, differences arise in trajectory distances as well as measured along-trajectory characteristics.

In general, ARs that make landfall in the western USA and ending at 1000 m MSL exhibit quasi-zonal orientations and cyclonic curvatures. They become less zonal and begin to extend in a northeastward orientation typical of ARs that make landfall in North America (e.g. Neiman et al. 2008a) at higher altitudes with SCA AR trajectories displaying more zonal orientations (e.g. Harris & Carvalho 2018). SCA ARs trajectories appear farther south and trajectory locations 72 h before landfall are farther eastward in Pacific, which is consistent with previous North American AR studies (Harris & Carvalho 2018). In the 72 h before landfall, very few AR trajectories travel below 30.0° N, which indicates that water vapor origins (within 72 h of landfall) of many ARs may not be tropical in nature, as ARs gather their water vapor through direct horizontal transport as well as local convergence (Bao et al. 2006). SCA ARs have the shortest trajectories at all levels, thus in the 72 h before landfall these ARs are slower. This suggests that these ARs may have differing relationships with extratropical cyclones or the influence of high topography on the progression of these ARs than their more northern counterparts.

With along-trajectory characteristics at all regions, parcels ending at 1000 and 2000 m MSL show moistening (1–3 g kg^{-1}) as well as subsidence (≤1.75 hPa hr^{-1}) along the early course of their trajectories (15–72 h). In the hours directly before landfall (0–15 h), there is a decrease in pressure, high (~70%) relative humidity values, and drops in specific humidity and temperature indicating orographic uplift.

Differences between ARs that make landfall in different regions show prominent differences lower in the atmosphere that lessen or diminish higher in the atmosphere. SCA AR trajectories ending at 1000 and 2000 m MSL tend to be warmer both with maximum along-trajectory temperatures (t_{max}) as well as landfall temperatures (t_{land}). This may be due in part to the occurrence of these ARs at lower latitudes. These

warmer temperatures also increase water's equilibrium vapor pressure indicating the AR's potential to 'hold' more moisture, as well as being more likely to result in rainfall as opposed to snow, at least upon initial landfall. In regard to specific humidity, for trajectories ending at 1000 m MSL, SCA ARs have higher moisture contents indicated through their maximum specific humidity values (q_{max}) as well as higher specific humidities at landfall (q_{land}) than both NCA and PNW ARs. At 2000 m MSL, this difference is only seen with SCA and PNW. The difference between maximum specific humidities and specific humidities at landfall (q_{delta}) show that SCA ARs experience the highest moisture losses over the course of their trajectories, but only significantly differ from PNW at 1000 and 3000 m MSL, with no differences found between any landfall region at 2000 m MSL or between SCA and NCA ARs. This may suggest the influence of topography on SCA ARs at lower altitudes and indicates that regardless of landfall location, at higher altitudes ARs are likely losing similar amounts of moisture due to condensation and precipitation along the course of their trajectories. These differences help to account for the variances seen with SCA ARs, which make landfall less frequently than their more northern counterparts but are still capable of extreme events.

An analysis of a strong February 2017 AR reveals a high-intensity storm with some characteristics that vary from typical ARs, indicating that this was an extreme event. IMERG precipitation data show rainfall throughout the state of California with a narrow band of high values corresponding with the AR in the pre-cold frontal area of the storm (Eiras-Barca et al. 2018). Reanalysis fields show that the day before SCA landfall, there is strong 850 mb flow and a corresponding plume of high TPW extending from Hawaii to southern Oregon and northern California. A frontal wave emerges and develops into a cyclone, shifting the axes of the offshore trough as well as augmenting moisture due to increased convergence. This channels moisture and winds to SCA. With the HYSPLIT analysis, this event differs from other SCA ARs in that trajectories remain at low altitudes and do not experience subsidence in the hours before landfall. This event has increased moisture values that surpass the 75th percentile of the other SCA ARs examined as well as higher maximum temperatures although temperatures at landfall are comparable to other SCA ARs. Over the course of 72 h these trajectories travel short distances, indicating that this event moved rather slowly in the hours before landfall. This combination of warm temperatures, slow movement, and high specific humidity values resulted in one of the most extreme regional storms seen in years. It also brings into question the future of other AR storms affecting SCA and how their intensity and duration may change under climate change scenarios (e.g. Dettinger 2011, Payne et al. 2020).

Understanding the differences of trajectories between ARs that make landfall in various areas is imperative to understanding AR manifestation and lifecycles. This is especially true for SCA ARs, which are infrequent, but responsible for high-intensity storms as well as large proportions of the regional annual precipitation totals. Knowing how the environment affects these events and how these episodes progress will be vital for future forecasts and hazard mitigation.

Acknowledgements. The authors gratefully acknowledge the NOAA Air Resources Laboratory for the provision of the HYSPLIT transport and dispersion model used in this publication. This project was funded in part by the University of California, Santa Barbara, Graduate Division. S.M.H. greatly appreciates many helpful discussions with Grant McKenzie who was crucial to HYSPLIT analysis.

LITERATURE CITED

Anderson TW, Finn JD (1996) The new statistical analysis of data. Springer-Verlag, New York, NY

Bao JW, Michelson SA, Neiman PJ, Ralph FM, Wilczak JM (2006) Interpretation of enhanced integrated water vapor bands associated with extratropical cyclones: their formation and connection to tropical moisture. Mon Weather Rev 134:1063–1080

Campmany E, Bech J, Rodríguez-Marcos J, Sola Y, Lorente J (2010) A comparison of total precipitable water measurements from radiosonde and sunphotometers. Atmos Res 97:385–392

Dettinger MD (2004) Fifty-two years of 'pineapple-express' storms across the west coast of North America. California Energy Commission PIER Energy-Related Environmental Research Report CEC-500-2005-004, California Energy Commission: Sacramento, CA

Dettinger MD (2011) Climate change, atmospheric rivers, and floods in California — a multimodel analysis of storm frequency and magnitude changes. J Am Water Resour Assoc 47:514–523

Dettinger MD, Ralph FM, Das T, Neiman PJ, Cayan DR (2011) Atmospheric rivers, floods, and the water resources of California. Water 3:445–478

Dettinger M, Ralph FM, Lavers D (2015) Setting the stage for a global science of atmospheric rivers. Eos (Wash DC) 96, doi:10.1029/2015EO038675

Draxler RR, Hess GD (1997) Description of the HYSPLIT_4 modeling system. NOAA Tech Memo ERL ARL-224

Draxler RR, Hess GD (1998) An overview of the HYSPLIT_4 modelling system for trajectories. Aust Meteorol Mag 47: 295–308

Eiras-Barca J, Ramos AM, Pinto JG, Trigo RM, Liberato MLR, Miguez-Macho G (2018) The concurrence of atmos-

pheric rivers and explosive cyclogenesis in the North Atlantic and North Pacific basins. Earth Syst Dynam 9: 91–102

Gershunov A, Shulgina T, Ralph FM, Lavers DA, Rutz JJ (2017) Assessing the climate-scale variability of atmospheric rivers affecting western North America. Geophys Res Lett 44:7900–7908

Gimeno L, Dominguez F, Nieto R, Trigo R and others (2016) Major mechanisms of atmospheric moisture transport and their role in extreme precipitation events. Annu Rev Environ Resour 41:117–141

Guan B, Waliser DE (2019) Tracking atmospheric rivers globally: spatial distributions and temporal evolution of life cycle characteristics. J Geophys Res Atmos 124: 12523–12552

Guan B, Molotch NP, Waliser DE, Fetzer EJ, Neiman PJ (2013) The 2010/11 snow season in California's Sierra Nevada: role of atmospheric rivers and modes of large-scale variability. Water Resour Res 49:6731–6743

Harris SM, Carvalho LMV (2018) Characteristics of Southern California atmospheric rivers. Theor Appl Climatol 132:965–981

Huffman GJ, Bolvin DT, Braithwaite D, Hsu K and others (2017) NASA global precipitation measurement (GPM) integrated multi-satellite retrievals for GPM (IMERG), algorithm theoretical basis document (ATBD) version 4.6. NASA/GSFC, Greenbelt, MD

Jiang T, Evans KJ, Deng Y, Dong X (2014) Intermediate frequency atmospheric disturbances: a dynamical bridge connecting western US extreme precipitation with East Asian cold surges. J Geophys Res Atmos 119: 3723–3735

Jones C, Carvalho LMV (2012) Spatial-intensity variations in extreme precipitation in the contiguous United States and the Madden-Julian Oscillation. J Clim 25: 4898–4913

Kanamitsu M (1989) Description of the NMC global data assimilation and forecast system. Weather Forecast 4: 335–342

Kim J, Waliser DE, Neiman PJ, Guan B, Ryoo JM, Wick GA (2013) Effects of atmospheric river landfalls on the cold season precipitation in California. Clim Dyn 40:465–474

Knippertz P, Martin JE (2007) A Pacific moisture conveyor belt and its relationship to a significant precipitation event in the semiarid southwestern United States. Weather Forecast 22:125–144

Knippertz P, Wernli H (2010) A Lagrangian climatology of tropical moisture exports to the Northern Hemispheric extratropics. J Clim 23:987–1003

Konrad CP, Dettinger MD (2017) Flood runoff in relation to water vapor transport by atmospheric rivers over the western United States, 1949–2015. Geophys Res Lett 44: 11456–11462

Lavers DA, Allan RP, Wood EF, Villarini G, Brayshaw DJ, Wade AJ (2011) Winter floods in Britain are connected to atmospheric rivers. Geophys Res Lett 38:L23803

Leung LR, Qian Y (2009) Atmospheric rivers induced heavy precipitation and flooding in the western US simulated by the WRF regional climate model. Geophys Res Lett 36:L03820

Martinković M, Mahović NS, Jurković PM, Renko T, Pelajić I, Smiljanić I (2017) Relationship between atmospheric rivers and extreme precipitation events. In: Karacostas TS, Bais AF, Nastos PT (eds) Perspectives on atmospheric sciences. Springer, Cham, p 385–390

Moore BJ, Neiman PJ, Ralph FM, Barthold FE (2012) Physical processes associated with heavy flooding rainfall in Nashville, Tennessee, and Vicinity during 1–2 May 2010: the role of an atmospheric river and mesoscale convective systems. Mon Weather Rev 140:358–378

Neiman PJ, Ralph FM, White AB, Kingsmill DE, Persson POG (2002) The statistical relationship between upslope flow and rainfall in California's coastal mountains: observations during CALJET. Mon Weather Rev 130:1468–1492

Neiman PJ, Ralph FM, Wick GA, Lundquist JD, Dettinger MD (2008a) Meteorological characteristics and overland precipitation impacts of atmospheric rivers affecting the West Coast of North America based on eight years of SSM/I satellite observations. J Hydrometeorol 9:22–47

Neiman PJ, Ralph FM, Wick GA, Kuo YH and others (2008b) Diagnosis of an intense atmospheric river impacting the Pacific Northwest: storm summary and offshore vertical structure observed with COSMIC satellite retrievals. Mon Weather Rev 136:4398–4420

Neiman PJ, Schick LJ, Ralph FM, Hughes M, Wick GA (2011) Flooding in western Washington: the connection to atmospheric rivers. J Hydrometeorol 12:1337–1358

Neiman PJ, Ralph FM, Moore BJ, Hughes M, Mahoney KM, Cordeira JM, Dettinger MD (2013) The landfall and inland penetration of a flood-producing atmospheric river in Arizona. I. Observed synoptic-scale, orographic, and hydrometeorological characteristics. J Hydrometeorol 14:460–484

Newell RE, Newell NE, Zhu Y, Scott C (1992) Tropospheric rivers? A pilot study. Geophys Res Lett 19:2401–2404

Newman M, Kiladis GN, Weickmann KM, Ralph FM, Sardeshmukh PD (2012) Relative contributions of synoptic and low-frequency eddies to time-mean atmospheric moisture transport, including the role of atmospheric rivers. J Clim 25:7341–7361

Oakley NS, Cannon F, Boldt E, Dumas J, Ralph FM (2018) Origins and variability of extreme precipitation in the Santa Ynez River Basin of Southern California. J Hydrol (Amst) 19:164–176

Payne AE, Magnusdottir G (2014) Dynamics of landfalling atmospheric rivers over the North Pacific in 30 years of MERRA reanalysis. J Clim 27:7133–7150

Payne AE, Demory ME, Leung LR, Ramos AM and others (2020) Responses and impacts of atmospheric rivers to climate change. Nat Rev Earth Environ 1:143–157

Ralph FM, Dettinger MD (2011) Storms, floods, and the science of atmospheric rivers. Eos (Wash DC) 92:265–272

Ralph FM, Dettinger MD (2012) Historical and national perspectives on extreme west coast precipitation associated with atmospheric rivers during December 2010. Bull Am Meteorol Soc 93:783–790

Ralph FM, Neiman PJ, Kingsmill DE, Persson POG and others (2003) The impact of a prominent rain shadow on flooding in California's Santa Cruz Mountains: a CALJET case study and sensitivity to the ENSO cycle. J Hydrometeorol 4:1243–1264

Ralph FM, Neiman PJ, Wick GA (2004) Satellite and CALJET aircraft observations of atmospheric rivers over the eastern North Pacific Ocean during the winter of 1997/98. Mon Weather Rev 132:1721–1745

Ralph FM, Neiman PJ, Rotunno R (2005) Dropsonde observations in low-level jets over the northeastern Pacific Ocean from CALJET-1998 and PACJET-2001: Mean vertical-profile and atmospheric-river characteristics. Mon Weather Rev 133:889–910

Ralph FM, Neiman PJ, Wick GA, Gutman SI, Dettinger MD, Cayan DR, White AB (2006) Flooding on California's Russian River: role of atmospheric rivers. Geophys Res Lett 33:L13801

Ralph FM, Neiman PJ, Kiladis GN, Weickmann K, Reynolds DW (2011) A multi-scale observational case study of a Pacific atmospheric river exhibiting tropical–extratropical connections and a mesoscale frontal wave. Mon Weather Rev 139:1169–1189

Ramos AM, Nieto R, Tomé R, Gimeno L, Trigo RM, Liberato MLR, Lavers DA (2016) Atmospheric rivers moisture sources from a Lagrangian perspective. Earth Syst Dynam 7:371–384

Rutz JJ, Steenburgh WJ (2012) Quantifying the role of atmospheric rivers in the interior western United States. Atmos Sci Lett 13:257–261

Rutz JJ, Steenburgh WJ, Ralph FM (2015) The inland penetration of atmospheric rivers over western North America: a Lagrangian analysis. Mon Weather Rev 143: 1924–1944

Saha S, Moorthi S, Pan HL, Wu X and others (2010) The NCEP climate forecast system reanalysis. Bull Am Meteorol Soc 91:1015–1057

Sodemann H, Stohl A (2013) Moisture origin and meridional transport in atmospheric rivers and their association with multiple cyclones. Mon Weather Rev 141:2850–2868

Stein AF, Draxler RR, Rolph GD, Stunder BJB, Cohen MD, Ngan F (2015) NOAA's HYSPLIT atmospheric transport and dispersion modeling system. Bull Am Meteorol Soc 96:2059–2077

Trenberth KE (1999) Atmospheric moisture recycling: role of advection and local evaporation. J Clim 12:1368–1381

Wang M, Wang J, Bock Y, Liang H, Dong D, Fang P (2019) Dynamic mapping of the movement of landfalling atmospheric rivers over southern California with GPS data. Geophys Res Lett 46:3551–3559

Wick GA, Neiman PJ, Ralph FM (2013) Description and validation of an automated objective technique for identification and characterization of the integrated water vapor signature of atmospheric rivers. IEEE Trans Geosci Remote Sens 51:2166–2176

Zhang C (2005) Madden-Julian Oscillation. Rev Geophys 43:RG2003

Zhu Y, Newell RE (1994) Atmospheric rivers and bombs. Geophys Res Lett 21:1999–2002

Zhu Y, Newell RE (1998) A proposed algorithm for moisture fluxes from atmospheric rivers. Mon Weather Rev 126: 725–735

Editorial responsibility: Oliver Frauenfeld, College Station, Texas, USA
Reviewed by: 3 anonymous referees

Submitted: March 27, 2020
Accepted: April 26, 2021
Proofs received from author(s): September 24, 2021